

# Graphene photodetectors with ultra-broadband and high responsivity at room temperature

Chang-Hua Liu<sup>1†</sup>, You-Chia Chang<sup>2†</sup>, Theodore B. Norris<sup>1,2\*</sup> and Zhaohui Zhong<sup>1\*</sup>

**The ability to detect light over a broad spectral range is central to several technological applications in imaging, sensing, spectroscopy and communication<sup>1,2</sup>. Graphene is a promising candidate material for ultra-broadband photodetectors, as its absorption spectrum covers the entire ultraviolet to far-infrared range<sup>3,4</sup>. However, the responsivity of graphene-based photodetectors has so far been limited to tens of  $\text{mA W}^{-1}$  (refs 5–10) due to the small optical absorption of a monolayer of carbon atoms. Integration of colloidal quantum dots in the light absorption layer can improve the responsivity of graphene photodetectors to  $\sim 1 \times 10^7 \text{ A W}^{-1}$  (ref. 11), but the spectral range of photodetection is reduced because light absorption occurs in the quantum dots. Here, we report an ultra-broadband photodetector design based on a graphene double-layer heterostructure. The detector is a phototransistor consisting of a pair of stacked graphene monolayers (top layer, gate; bottom layer, channel) separated by a thin tunnel barrier. Under optical illumination, photoexcited hot carriers generated in the top layer tunnel into the bottom layer, leading to a charge build-up on the gate and a strong photogating effect on the channel conductance. The devices demonstrated room-temperature photodetection from the visible to the mid-infrared range, with mid-infrared responsivity higher than  $1 \text{ A W}^{-1}$ , as required by most applications<sup>12</sup>. These results address key challenges for broadband infrared detectors, and are promising for the development of graphene-based hot-carrier optoelectronic applications.**

Today, different technologically important wavelength regimes are detected by separate photoactive semiconductors with appropriate bandgaps. For example, GaN, silicon and InGaAs are typically exploited for sensing in the ultraviolet, visible and near-infrared regimes, respectively, whereas the detection of mid-infrared photons generally relies on small-bandgap semiconductor compounds such as HgCdTe, PbS or PbSe, and thermal sensing techniques are utilized for detection in the far-infrared regime. In contrast to these materials, graphene is a promising optoelectronic material for ultra-broadband photodetectors due to its gapless bandstructure<sup>3,4</sup>. The difficulty with utilizing graphene in standard photodetector structures is that the lifetime of photogenerated carriers is very short, and it is therefore necessary to separate the electrons and holes on a sub-picosecond timescale in order to efficiently generate a photocurrent and avoid simple heating of the graphene layer. So far, nearly all graphene-based photodetectors focus on exploiting graphene–metal junctions or graphene p–n junctions for extracting photocurrent<sup>5–8,13–15</sup>. Unfortunately, these sensing schemes suffer from the small area of the effective junction region contributing to the photocurrent, as well as weak optical absorption, and the responsivity is therefore limited to a few  $\text{mA W}^{-1}$ . Integrating graphene with plasmonic nanostructures<sup>16–18</sup> or microcavities<sup>19,20</sup> can enhance

the light–graphene interaction and improve the responsivity to tens of  $\text{mA W}^{-1}$ . However, the enhancement can only be achieved at the designed resonant frequencies, restricting their applications for broadband photodetection. With this in mind, the idea of silicon waveguide-integrated graphene photodetectors was recently proposed, demonstrating broadband photodetection with enhanced responsivity to tens of  $\text{mA W}^{-1}$  (refs 19,20). Photoresponsivity above  $0.1 \text{ A W}^{-1}$  can also be achieved in transition-metal dichalcogenide/graphene stacks by exploiting the strong light–matter interaction<sup>21</sup>. Bandstructure engineering in graphene has also recently been explored for photoresponsivity enhancement<sup>22</sup>, but efficient photodetection can only be achieved below  $\sim 150 \text{ K}$  due to the short electron lifetime in midgap states at elevated temperatures.

An alternative approach is to exploit photoconductive gain in graphene. Although graphene is conventionally regarded as a poor photoconductor because of its ultrafast hot carrier recombination<sup>23–26</sup>, recent studies have demonstrated that hybridized graphene/quantum-dot photodetectors can achieve high photoconductive gain<sup>11,27</sup>. This sensitive detection scheme is attributed to a strong photogating effect induced by trapped photocarriers in the quantum dots. Despite the excellent device responsivity, light absorption relies on the quantum dots instead of the graphene, thus restricting the spectral range of photodetection.

In this Letter we present a graphene-based ultra-broadband photodetector composed of two graphene layers sandwiching a thin tunnel barrier. In contrast to conventional phototransistors as well as lateral graphene devices<sup>13,15,28</sup>, hot electrons and holes are separated in our structure by selective quantum tunnelling into opposite graphene layers, thereby minimizing hot carrier recombination. The trapped charges on the top graphene layer can result in a strong photogating effect on the bottom graphene channel layer, yielding an unprecedented photoresponsivity over an ultra-broad spectral range. By engineering a proper tunnel barrier, we demonstrate prototype devices achieving ultra-broadband photodetection and a room-temperature mid-infrared responsivity comparable with state-of-the-art infrared photodetectors operating at low temperature<sup>29</sup>.

The working principle of the graphene double-layer heterostructure photodetector can be understood through the device schematic and band diagram in Fig. 1a,c. The device is composed of two graphene layers sandwiching a thin tunnel barrier, in this case 5-nm-thick  $\text{Ta}_2\text{O}_5$  (see Methods). The graphene functions not only as the charge transport channel but also as the light absorber. The intrinsic doping level and Fermi energy of the bottom graphene layer can be readily determined by the backgate voltage ( $V_{\text{gb}}$ )-dependent transfer curve (Fig. 1b, black curve, see also Supplementary Fig. 2). To determine the Fermi energy of the top graphene layer, we can operate the bottom graphene layer as a

<sup>1</sup>Department of Electrical Engineering and Computer Science, University of Michigan, 1301 Beal Avenue, Ann Arbor, Michigan 48109, USA, <sup>2</sup>Center for Ultrafast Optical Science, University of Michigan, 1006 Gerstacker Building, 2000 Bonisteel Boulevard, Ann Arbor, Michigan 48109, USA. <sup>†</sup>These authors contributed equally to this work. \*e-mail: zzhong@umich.edu; tnnorris@umich.edu

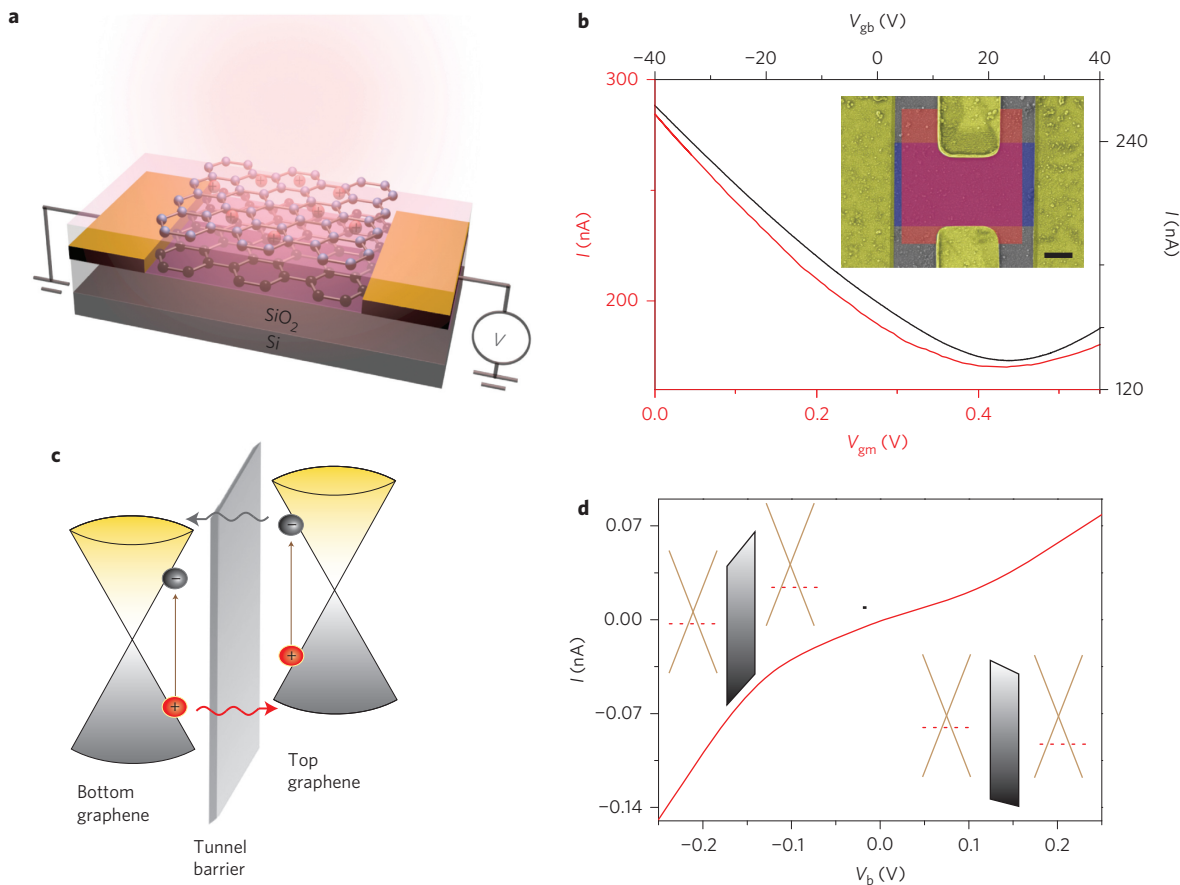


**Figure 1 | Graphene double-layer heterostructure photodetectors.** **a**, Schematic of device structure. **b**, Black (right and top axes): transfer curve for bottom graphene layer using a silicon backgate ( $V_{gb}$ ). Red (left and bottom axes): transfer curve for top graphene layer using the bottom graphene as the gate ( $V_{gm}$ ). From these transport curves, we calculate the Fermi energies of the top and bottom graphene layers to be 4.756 eV and 4.655 eV, respectively. Inset: False-colour scanning electron microscopy (SEM) image of the device. The gold areas indicate the metal electrodes and the purple and red areas the bottom and top graphene layers, respectively. Scale bar, 1  $\mu\text{m}$ . **c**, Schematic of band diagram and photoexcited hot carrier transport under light illumination. Electrons and holes are represented by grey and red spheres, respectively. Vertical arrows represent photoexcitation, and lateral arrows represent tunnelling of hot electron (grey) and hole (red). **d**, Vertical tunnelling current as a function of bias voltage applied across two graphene layers. The bottom layer is grounded, and bias voltage is applied to the top layer. Inset: Schematic band diagrams under forward and reverse bias. Red dashed lines indicate the Fermi levels of the graphene layers.

gate ( $V_{gm}$ ) and measure its gate effect on the top graphene layer (Fig. 1b, red curve). The top graphene layer was found to be more heavily p-doped relative to the bottom graphene layer, with an average Fermi energy difference of 0.12 eV (Supplementary Sections 1 and 2). Therefore, the energy band of the tunnelling barrier is tilted toward the bottom graphene layer in order to equilibrate the Fermi level (Fig. 1c). Critically, these two closely spaced graphene layers are electrically isolated, with an interlayer resistance of  $>4 \text{ G}\Omega$ . The tunnelling dark current can be measured by applying a bias voltage across the graphene double layer, as shown in Fig. 1d. The  $I$ - $V$  characteristics show a larger magnitude of tunnelling current in the negative bias region than in the positive bias region, also in agreement with the asymmetry of the tunnel barrier depicted in Fig. 1c.

For typical photodetection operation, the potential of the top graphene layer is allowed to float while the light-induced conductance change of the bottom graphene layer is measured in the bottom graphene layer transistor. Under light illumination, photoexcited hot carriers can tunnel efficiently into the nearby graphene layer. Most importantly, the asymmetric tunnelling barrier favours hot electrons tunnelling from the top to the bottom graphene layer. As a result, positive charges accumulate in the top graphene layer, leading to a photogating effect on the bottom graphene transistor. In particular,

the graphene channel has high carrier mobility and is very sensitive to external electrostatic perturbation, while the thin oxide film in this device design not only favours hot carrier tunnelling, but also induces high interlayer dielectric capacitance. All these factors contribute to a strong photogating effect and lead to efficient photon detection.

To confirm the above mechanism, we next turned our attention to the photoresponse of the graphene photodetector. Figure 2a shows the effect of light illumination (continuous-wave,  $\lambda = 532 \text{ nm}$ ) on the gate response of the bottom graphene transistor over four orders of magnitude optical power. Interestingly, the transfer curve shifts dramatically toward negative  $V_{gb}$  with increasing laser power, and a Dirac point voltage shift of 40 V is observed (Fig. 2c, inset). This observation supports the proposed detection mechanism; that is, efficient tunnelling of high-energy hot electrons leads to positive charge build-up in the top graphene layer, giving rise to a strong photogating effect and n-doping of the bottom graphene channel (Fig. 2a, inset). The net photocurrent can be obtained by subtracting the dark current from the light current ( $I_{\text{light}} - I_{\text{dark}}$ ), and is plotted in Fig. 2b. It is clear that the magnitude of photocurrent increases with excitation power. More importantly, the photocurrent signal can be gate-modulated, offering convenient on-off switching control for photodetection.

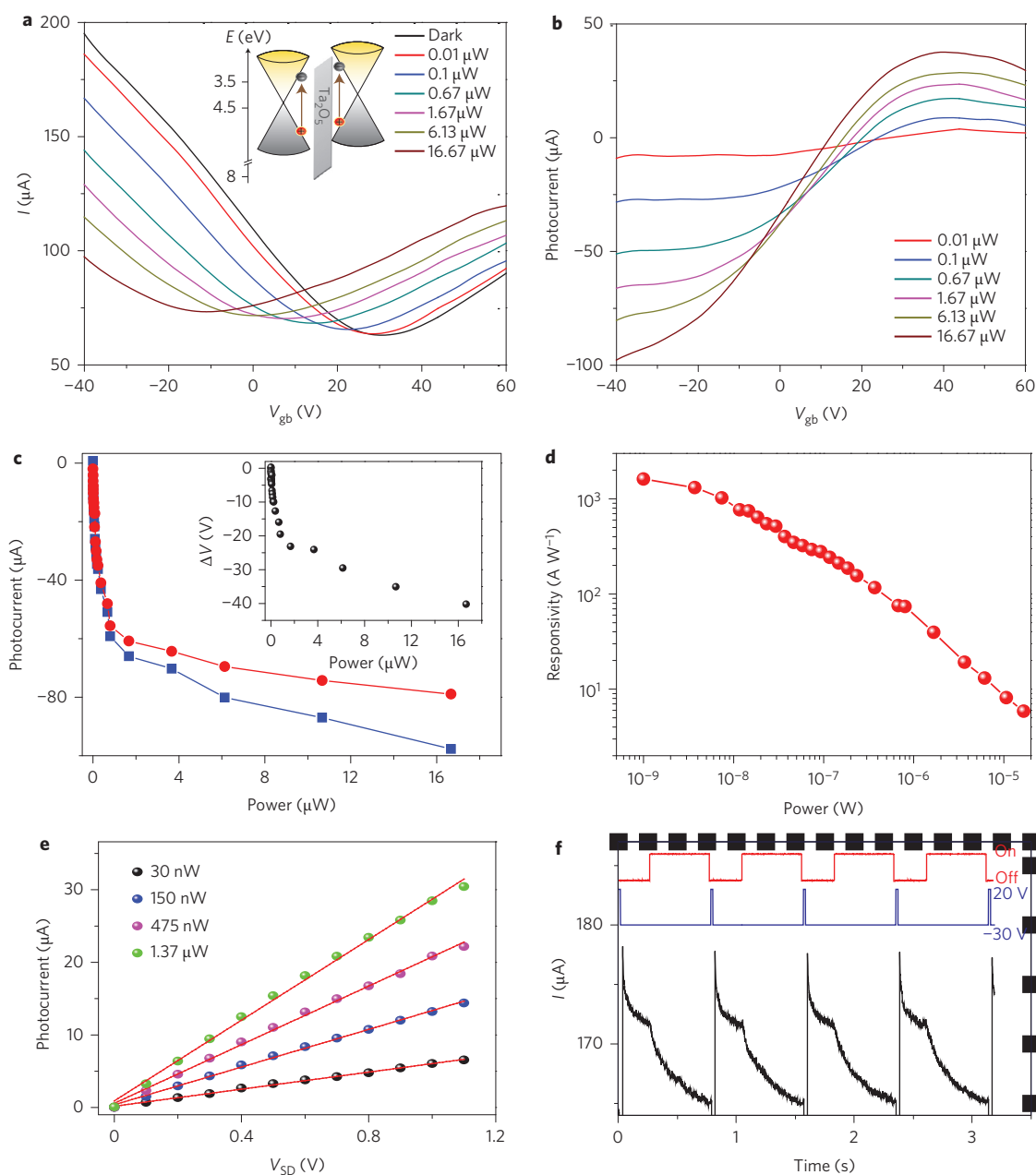


**Figure 2 | Photoresponse of the graphene double-layer heterostructures in the visible region.** **a**,  $I$ - $V_{gb}$  characteristics of the measured graphene photodetector under different laser powers. The potential of the top graphene layer was allowed to float, while the current of the bottom graphene transistor was measured under 1 V source-drain bias voltage. The laser wavelength is 532 nm with a spot size of 10  $\mu\text{m}$ , covering the entire graphene photodetector. Inset: Energy band diagram of the graphene/ $\text{Ta}_2\text{O}_5$ /graphene heterostructures. **b**, Gate dependence of photocurrent under different laser powers. **c**, Power dependence of photocurrent at  $-40$  V (blue squares) and  $-20$  V (red circles) backgate voltages. Inset: Shift of Dirac point gate voltages as a function of illumination power. **d**, Measured photoresponsivity versus illumination power. Red lines are linear fits.  $V_{gb} = 0$  V. **e**, The magnitude of the photocurrent increases linearly with source-drain bias voltage of the bottom graphene layer transistor. Red lines are linear fits.  $V_{gb} = 0$  V. **f**, Temporal photoresponse of the graphene photodetector (black curve). The illumination power is 0.3  $\mu\text{W}$  and the laser wavelength is 532 nm. The laser on-off (red curve) is controlled by a mechanical shutter synchronized with the reset backgate voltage pulses (blue curve).

The noise properties in this device design are determined mainly by the dark current in the conducting channel. We measured the frequency-dependent noise spectral density of the photodetector under 1 V bias (Supplementary Fig. 3), and found that a room-temperature noise equivalent power (NEP) of  $\sim 1 \times 10^{-11} \text{ W Hz}^{-1/2}$  at 1 Hz is achieved in our proof-of-concept device (Supplementary Section 3).

To gain further insight into the characteristics of this photodetector, we extracted the power dependence of the current

(Fig. 2c) and calculated the responsivity of the device (Fig. 2d). Under low excitation power, the device shows a remarkable responsivity of greater than 1,000  $\text{A W}^{-1}$  at 1 V source-drain bias voltage ( $V_{SD}$ ), suggesting that the built-in amplification mechanism can efficiently convert the photon energy into a large electrical signal. In addition, the photo-induced current also shows a linear dependence on the bias voltage (Fig. 2e), suggesting higher responsivity can be readily achieved by applying a larger bias voltage. The time-dependent photo-induced current measurement under

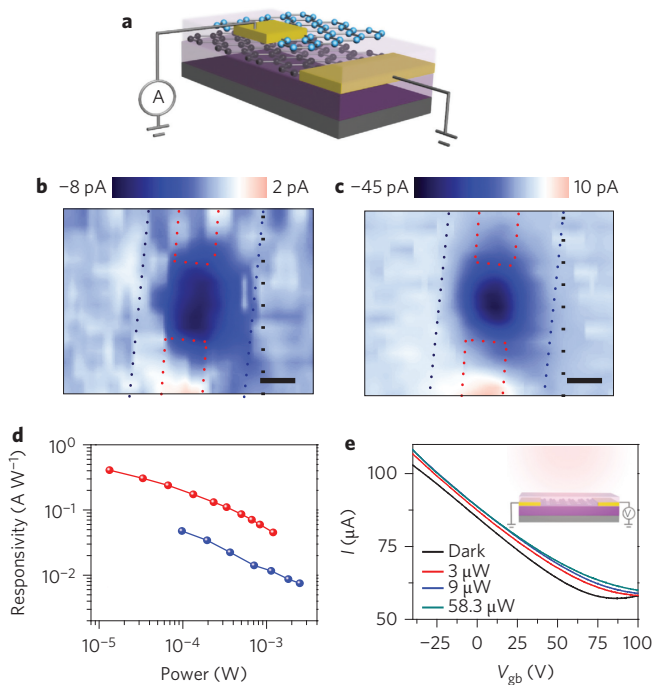


**Figure 3 | Photoexcited hot carrier tunnelling in graphene double-layer heterostructures.** **a**, Schematic of electrical measurement set-up for scanning photocurrent imaging. Photocurrent across the two graphene layers is directly measured to confirm the photoexcited hot carrier tunnelling mechanism. **b,c**, Scanning photocurrent images of the graphene double-layer heterostructures at excitation wavelengths of 900 nm (**b**) and 800 nm (**c**). Blue dotted lines indicate the edges of the bottom electrodes and red dotted lines the edges of the top electrodes. Vertical tunnelling current across the heterostructures was measured under the short-circuit condition with the bottom graphene layer grounded. The laser spot size for these scanning measurements was  $\sim 1.5 \mu\text{m}$ , and the laser power was 1 mW. Scale bars,  $2 \mu\text{m}$ . **d**, Responsivity comparison of graphene photodetector at wavelengths of 800 nm (red) and 900 nm (blue). **e**, Photoresponse of a control device with identical design, except for the absence of the top graphene layer. Inset: Schematic of control device.

on–off light modulation was also performed with 1 V bias voltage at room temperature (Fig. 2f). A reset gate voltage pulse of 10 ms was used for fast switching<sup>11</sup> and a current modulation of  $7 \mu\text{A}$  was clearly evident. We note that the speed of our proof-of-concept devices is limited at 10–1,000 Hz, probably due to charge trap states in the sputtered tunnelling barrier. Because the fundamental hot carrier tunnelling rate is less than a picosecond, we expect that significant improvement may be obtained with better dielectric quality.

To further confirm the hot carrier tunnelling mechanism, we performed scanning photocurrent spectroscopy<sup>5,6,13</sup> and directly measured the hot carrier tunnelling current across the graphene layers. The tunnelling current due to photoexcitation was measured under the short-circuit condition with the bottom graphene layer grounded (Fig. 3a). Figure 3b shows a scanning photocurrent image of the device under continuous-wave laser excitation at 900 nm. The result clearly shows that photocurrent is generated within the overlapped region of two graphene layers instead of at the graphene–metal junctions (Supplementary Section 4), suggesting that the charge separation arises from hot carrier tunnelling and not at the graphene–metal junctions as in conventional graphene detectors. Additionally, the photocurrent polarity is negative, providing direct evidence that the asymmetry of the tunnel barrier facilitates hot electron transport from the top to the

bottom graphene layer. Furthermore, we measured the same device with a shorter irradiation wavelength at 800 nm. A scanning photocurrent map shows qualitatively similar features, but nearly six times larger photocurrent compared with 900 nm excitation at the same laser intensity (Fig. 3c). The dependence of photocurrent on photon energy provides further support for hot carrier tunnelling, because carriers excited to higher energies should have a higher injection rate through the barrier<sup>30</sup>. We also emphasize that the direct photocurrent tunnelling current between the two graphene layers is seven orders of magnitude smaller than the photogating effect shown in Fig. 2 (10 pA versus  $100 \mu\text{A}$ ). This result further highlights the advantage of utilizing the photogating effect of the top graphene layer for high-responsivity photodetection.

The measured wavelength-dependent photoresponsivities of the graphene photodetector further support the concept that the responsivity is directly related to the photon energy dependence of the hot carrier tunnelling rate. As shown in Fig. 3d, photoresponsivities of the graphene photodetector at 800 nm are also about six times greater than at 900 nm (Supplementary Fig. 5), suggesting that the device responsivity is closely related to hot carrier injection rate. As control experiments, we also measured the photoresponse of a graphene transistor covered by 5-nm-thick  $\text{Ta}_2\text{O}_5$  but without the top graphene layer. As shown in Fig. 3e, the transfer curve shifts are much smaller and, most importantly, in the opposite direction when compared with the photoresponse of the graphene double-layer photodetector (Fig. 2a). This striking difference reveals the central role of the top graphene layer for both light absorption and photogating.

The tunnel barrier height is a key parameter affecting device operation. To extend the range of high-responsivity photodetection into the infrared regime we fabricated similar device structures, but incorporated intrinsic silicon as the tunnel barrier in place of the wide-bandgap  $\text{Ta}_2\text{O}_5$  layer. The silicon conduction band is  $\sim 0.5 \text{ eV}$  above the Fermi level of intrinsic graphene<sup>31</sup> (Fig. 4d, inset), enabling tunnelling of lower-energy electrons. The infrared photoresponses of the graphene/silicon/graphene heterostructures are similar to our previous measurements, displaying large shifts of the transfer curve and Dirac point voltage towards negative  $V_{\text{gb}}$  with increasing illumination power (Supplementary Fig. 6). Figure 4a–c shows the extracted gate dependence of photocurrent under 1.3  $\mu\text{m}$ , 2.1  $\mu\text{m}$  and 3.2  $\mu\text{m}$  wavelength light illumination, respectively. The strong photogating effect and gate modulation of the photosignal are again clearly observed in both near-infrared and mid-infrared regimes. Power-dependent photocurrent curves were extracted from Fig. 4a–c and are plotted in Fig. 4d–f, respectively. Significantly, the near-infrared responsivity of the device reaches  $4 \text{ A W}^{-1}$  at  $\lambda = 1.3 \mu\text{m}$  (Fig. 4d) and  $1.9 \text{ A W}^{-1}$  at  $\lambda = 2.1 \mu\text{m}$  (Fig. 4e) at room temperature. These values are more than three orders of magnitude higher than the responsivity of graphene/ $\text{Ta}_2\text{O}_5$ /graphene heterostructures at near-infrared wavelengths (Supplementary Fig. 5). Furthermore, our prototype graphene photodetector exhibits a room-temperature mid-infrared responsivity of  $1.1 \text{ A W}^{-1}$  at  $\lambda = 3.2 \mu\text{m}$  (Fig. 4f), rivalling state-of-the-art mid-infrared detectors without the need for cryogenic cooling.

In summary, hot carrier tunnelling as a mechanism for photo-detection in a graphene double-layer heterostructure provides a viable route for ultra-broadband and high-sensitivity photo-detection at room temperature. To further enhance device performance, the bottom graphene channel could be replaced with other thin-film semiconductors to reduce the background current. Furthermore, interlayer hot carrier tunnelling and photogating could be enhanced by utilizing atomically thin two-dimensional semiconductors such as  $\text{MoS}_2$  and  $\text{WS}_2$  as the tunnelling barrier layer<sup>32</sup>.

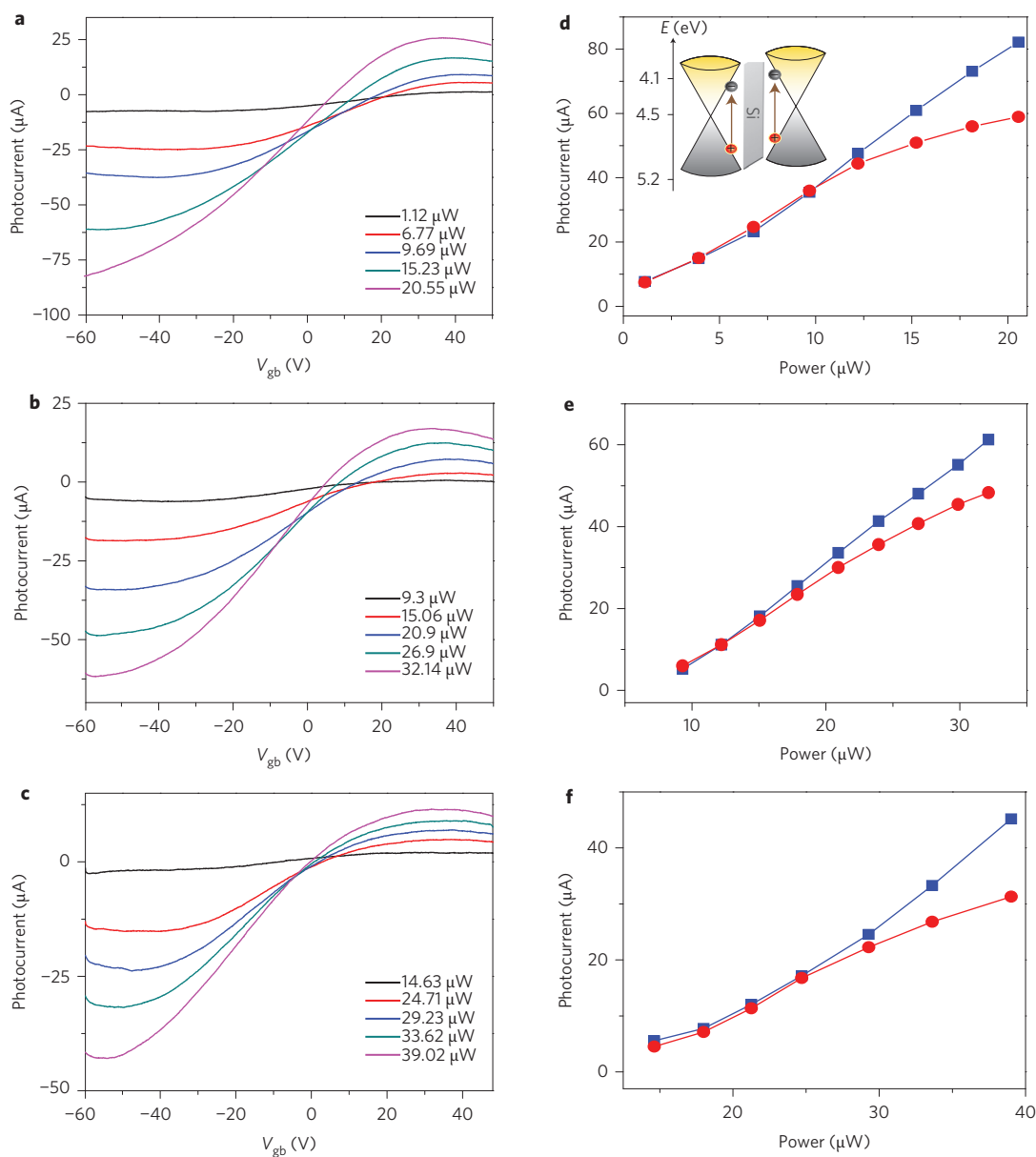


**Figure 4 | Near- to mid-infrared photoresponse of the graphene/silicon/graphene heterostructure photodetector.** **a–c**, Gate dependence of photocurrent under different illumination powers with excitation wavelengths at 1.3  $\mu\text{m}$  (**a**), 2.1  $\mu\text{m}$  (**b**) and 3.2  $\mu\text{m}$  (**c**). Measurements were conducted by applying 1.5 V bias voltage to the bottom graphene transistor, and the laser spots were focused to  $\sim 20$   $\mu\text{m}$ , covering the entire graphene photodetector. **d–f**, Photocurrent versus illumination power under excitation wavelengths of 1.3  $\mu\text{m}$  (**d**), 2.1  $\mu\text{m}$  (**e**) and 3.2  $\mu\text{m}$  (**f**). Representative curves with backgate voltages set at  $-60$  V (blue squares) and  $-30$  V (red circles) are shown. Inset in **d**: band diagram of graphene/silicon/graphene heterostructures.

## Methods

**Device fabrication.** The graphene films used in this work were grown by chemical vapour deposition (CVD) on copper foil and then transferred onto a Si/SiO<sub>2</sub> substrate<sup>33</sup>. The single-layer nature of the graphene films was confirmed by Raman spectroscopy. To fabricate graphene/Ta<sub>2</sub>O<sub>5</sub>/graphene heterostructures, we first transferred a graphene film onto a degenerately p-doped silicon wafer with 285 nm thermal oxide. Photolithography, graphene plasma etching and metal lift-off processes were used to fabricate the bottom graphene transistor. The sample was then covered by a 5-nm-thick Ta<sub>2</sub>O<sub>5</sub> film as the tunnel barrier, blanket-deposited by radiofrequency sputtering. Finally, the top graphene layer was transferred on top of the Ta<sub>2</sub>O<sub>5</sub> thin film, and subsequent photolithography, graphene etching and metal lift-off processes were used to fabricate the top graphene transistor. To fabricate the graphene/silicon/graphene heterostructures, we followed the same procedure, except replacing Ta<sub>2</sub>O<sub>5</sub> with 6 nm intrinsic silicon film deposited by sputtering.

**Light sources and power calibrations.** In this work, 532 nm, 800 nm and 900 nm wavelength light was generated from different continuous-wave semiconductor diode lasers and the laser power was calibrated by a silicon photodetector

(Newport, 918-SL-OD3R). For longer-wavelength measurements, the light source was provided by an optical parametric amplification (OPA) and difference frequency generation (DFG) system. The OPA was pumped by a 250 kHz amplified Tisapphire laser (Coherent, RegA 9000), generating signal and the idler waves at wavelengths of 1.3  $\mu\text{m}$  and 2.1  $\mu\text{m}$ , respectively. Both waves were sent to the DFG to produce light with a wavelength of 3.2  $\mu\text{m}$ . A zinc selenite aspherical lens was used to focus the infrared light to the device. The power was measured by an InGaAs detector (Thorlabs DET10D) at 1.3  $\mu\text{m}$  and 2.1  $\mu\text{m}$  and by an InSb detector (Infrared Associates, IS-2.0) at 3.2  $\mu\text{m}$ . Both detectors were calibrated by a thermopile broadband power meter (Melles Griot, 13PEM001).

Received 29 May 2013; accepted 28 January 2014;  
published online 16 March 2014

## References

- Rogalski, A. Infrared detectors: status and trends. *Prog. Quant. Electron.* **27**, 59–210 (2003).
- Clark, J. & Lanzani, G. Organic photonics for communications. *Nature Photon.* **4**, 438–446 (2010).

3. Nair, R. R. *et al.* Fine structure constant defines visual transparency of graphene. *Science* **320**, 1308 (2008).
4. Mak, K. F., Ju, L., Wang, F. & Heinz, T. F. Optical spectroscopy of graphene: from the far infrared to the ultraviolet. *Solid State Commun.* **152**, 1341–1349 (2012).
5. Park, J., Ahn, Y. H. & Ruiz-Vargas, C. Imaging of photocurrent generation and collection in single-layer graphene. *Nano Lett.* **9**, 1742–1746 (2009).
6. Xia, F. N. *et al.* Photocurrent imaging and efficient photon detection in a graphene transistor. *Nano Lett.* **9**, 1039–1044 (2009).
7. Xia, F. N., Mueller, T., Lin, Y. M., Valdes-Garcia, A. & Avouris, P. Ultrafast graphene photodetector. *Nature Nanotech.* **4**, 839–843 (2009).
8. Mueller, T., Xia, F. N. A. & Avouris, P. Graphene photodetectors for high-speed optical communications. *Nature Photon.* **4**, 297–301 (2010).
9. Gan, X. *et al.* Chip-integrated ultrafast graphene photodetector with high responsivity. *Nature Photon.* **7**, 888–891 (2013).
10. Pospischil, A. *et al.* CMOS-compatible graphene photodetector covering all optical communication bands. *Nature Photon.* **7**, 892–896 (2013).
11. Konstantatos, G. *et al.* Hybrid graphene–quantum dot phototransistors with ultrahigh gain. *Nature Nanotech.* **7**, 363–368 (2012).
12. Novoselov, K. S. *et al.* A roadmap for graphene. *Nature* **490**, 192–200 (2012).
13. Liu, C. H., Dissanayake, N. M., Lee, S., Lee, K. & Zhong, Z. H. Evidence for extraction of photoexcited hot carriers from graphene. *ACS Nano* **6**, 7172–7176 (2012).
14. Xu, X. D., Gabor, N. M., Alden, J. S., van der Zande, A. M. & McEuen, P. L. Photo-thermoelectric effect at a graphene interface junction. *Nano Lett.* **10**, 562–566 (2010).
15. Gabor, N. M. *et al.* Hot carrier-assisted intrinsic photoresponse in graphene. *Science* **334**, 648–652 (2011).
16. Echtermeyer, T. J. *et al.* Strong plasmonic enhancement of photovoltage in graphene. *Nature Commun.* **2**, 458 (2011).
17. Fang, Z. *et al.* Graphene-antenna sandwich photodetector. *Nano Lett.* **12**, 3808–3813 (2012).
18. Grigorenko, A. N., Polini, M. & Novoselov, K. S. Graphene plasmonics. *Nature Photon.* **6**, 749–758 (2012).
19. Furchi, M. *et al.* Microcavity-integrated graphene photodetector. *Nano Lett.* **12**, 2773–2777 (2012).
20. Engel, M. *et al.* Light–matter interaction in a microcavity-controlled graphene transistor. *Nature Commun.* **3**, 906 (2012).
21. Britnell, L. *et al.* Strong light–matter interactions in heterostructures of atomically thin films. *Science* **340**, 1311–1314 (2013).
22. Zhang, B. Y. *et al.* Broadband high photoresponse from pure monolayer graphene photodetector. *Nature Commun.* **4**, 1811 (2013).
23. Breusing, M., Ropers, C. & Elsaesser, T. Ultrafast carrier dynamics in graphite. *Phys. Rev. Lett.* **102**, 086809 (2009).
24. Freitag, M., Low, T., Xia, F. & Avouris, P. Photoconductivity of biased graphene. *Nature Photon.* **7**, 53–59 (2013).
25. Graham, M. W., Shi, S. F., Ralph, D. C., Park, J. & McEuen, P. L. Photocurrent measurements of supercollision cooling in graphene. *Nature Phys.* **9**, 103–108 (2013).
26. Brida, D. *et al.* Ultrafast collinear scattering and carrier multiplication in graphene. *Nature Commun.* **4**, 1987 (2013).
27. Sun, Z. *et al.* Infrared photodetectors based on CVD-grown graphene and PbS quantum dots with ultrahigh responsivity. *Adv. Mater.* **24**, 5878–5883 (2012).
28. Song, J. C. W., Rudner, M. S., Marcus, C. M. & Levitov, L. S. Hot carrier transport and photocurrent response in graphene. *Nano Lett.* **11**, 4688–4692 (2011).
29. Konstantatos, G. & Sargent, E. H. Nanostructured materials for photon detection. *Nature Nanotech.* **5**, 391–400 (2010).
30. Thissen, P., Schindler, B., Diesing, D. & Hasselbrink, E. Optical response of metal–insulator–metal heterostructures and their application for the detection of chemi-currents. *New J. Phys.* **12**, 113014 (2010).
31. Li, X. *et al.* Graphene-on-silicon Schottky junction solar cells. *Adv. Mater.* **22**, 2743–2748 (2010).
32. Georgiou, T. *et al.* Vertical field-effect transistor based on graphene–WS<sub>2</sub> heterostructures for flexible and transparent electronics. *Nature Nanotech.* **8**, 100–103 (2013).
33. Lee, S., Lee, K., Liu, C.-H. & Zhong, Z. Homogeneous bilayer graphene film based flexible transparent conductor. *Nanoscale* **4**, 639–644 (2012).

### Acknowledgements

The authors thank C.Y. Sung for discussions. This work was supported by the National Science Foundation (NSF) Center for Photonic and Multiscale Nanomaterials (DMR 1120923) and by a NSF CAREER Award (ECCS-1254468). Devices were fabricated in the Lurie Nanofabrication Facility at the University of Michigan, a member of the NSF National Nanotechnology Infrastructure Network.

### Author contributions

C.L., Z.Z. and T.N. conceived the experiments. C.L. fabricated the devices. C.L. and Y.C. performed the measurements. All authors discussed the results and co-wrote the manuscript.

### Additional information

Supplementary information is available in the [online version](#) of the paper. Reprints and permissions information is available online at [www.nature.com/reprints](http://www.nature.com/reprints). Correspondence and requests for materials should be addressed to T.B.N. and Z.Z.

### Competing financial interests

The University of Michigan at Ann Arbor, along with the authors, has filed provisional patents on the technology and intellectual property reported here (patent application number US 61/778,716; title: Photodetector based on double layer heterostructures).